ACCSCIENCE PUBLISHING

Engineering Science in Additive Manufacturing

ORIGINAL RESEARCH ARTICLE

Dimensional accuracy and surface roughness of thin-wall geometries in laser powder bed fusion of 316L stainless steel

Tianyu Zhang and Lang Yuan*

Department of Mechanical Engineering, Molinaroli College of Engineering and Computing, University of South Carolina, Columbia, South Carolina, United States of America

Abstract

Thin-wall geometries produced by laser powder bed fusion combine high manufacturing efficiency, design flexibility, and cost-effectiveness for specialized applications. In such features, surface quality directly impacts dimensional accuracy and functional performance. This study investigates the effects of laser power, scan path, build orientation, and nominal gap distance on the top- and vertical-surface roughness, surface features, and dimensional error (DE) of 316L stainless steel thin walls. Optical microscopy was employed to characterize melt pool morphology and surface characteristics. Increasing laser power enlarges melt pools, promotes lateral migration, and induces dross formation on vertical surfaces, raising roughness and DE. Incorporating a contour scan with an inward offset reduces the scanned area, limits melt pool migration, and improves dimensional accuracy. Print orientation has a negligible influence on DE under the tested conditions, while small gaps may close entirely at high power due to large melt pools and migration. Compared to cubes fabricated with identical parameters, thin walls exhibit rougher top surfaces at high power, attributed to reduced track overlap, limited wetting from previous layers, and powder redistribution near vertical edges, whereas vertical-surface behavior remains similar. These findings provide practical guidelines for optimizing dimensional accuracy and surface quality in thin walls through coordinated control of process parameters and geometry.

Keywords: Additive manufacturing; Thin-wall structures; Surface roughness; Dimensional accuracy; Melt pool migration

***Corresponding author:**
Lang Yuan
(langyuan@cec.sc.edu)

Citation: Zhang T, Yuan L. Dimensional accuracy and surface roughness of thin-wall geometries in laser powder bed fusion of 316L stainless steel. *Eng Sci Add Manuf*. 2025;1(3):025340022. doi: 10.36922/ESAM025340022

Received: August 19, 2025

Revised: August 27, 2025

Accepted: August 28, 2025

Published online: September 10, 2025

1. Introduction

Laser powder bed fusion (LPBF) has emerged as one of the leading metal additive manufacturing processes, due to its geometric flexibility and ability to deliver high-performance components.[1-4] It is particularly advantageous for fabricating unique thin-wall structures commonly used in industrial applications, such as turbines and heat exchangers, to achieve optimal performance.[5-8] In such features, side-wall surface roughness and topography critically affect the dimensional accuracy, such as the intervening feature distances[9] and functional and structural performance.[10-12] For example, uneven surfaces increase the contact area between the fluid and the thin-wall structures, thereby influencing heat transfer efficiency in heat exchangers.[13-15]

Likewise, irregular channel morphologies modify fluid resistance and permeability, affecting performance in applications such as turbines and nozzles.[16,17]

Prior research has shown that surface features and roughness are strongly governed by fabrication parameters.[18-20] Feng *et al.*[21] investigated the evolution of surface features in overhang regions of 17-4 precipitation hardening stainless steel. They reported that the dominant downward surface features transitioned from powder adhesion to powder clusters, warped deformation, and dross formation as the overhang angle increased. A similar progression was observed by Zhang and Yuan,[22] where the domination feature shifted from bare melt tracks with partially melted particles to pronounced dross as energy density increased. In related parametric studies, Klingaa *et al.*[23,24] revealed that surface roughness and its variation decrease with the increasing orientation angle due to a reduction of sintered particles on the surfaces. Beyond orientation angles, Gockel *et al.*[25] investigated the effect of contour power and speed on vertical surface roughness in alloy 718 pillar samples, finding that higher scan speeds promote melt pool instability and balling, thereby elevating roughness. With a further understanding of contour–hatch interactions, Patel *et al.*[26] demonstrated that contour and hatch parameters have a comparable impact on side-skin quality in Ti-6Al-4V cylinders through attached particles, spatter, and balling.

To deepen the understanding of the factors influencing dimensional accuracy and surface roughness in thin-wall geometries, previous work has examined pulsed-laser operation, geometric design, alloy composition, and scan strategy. For example, Mumtaz and Hopkinson[27] investigated the use of pulsed lasers on Inconel 625 in LPBF. They revealed that a ramp-down pulsed laser improved the top surface quality but negatively impacted the vertical surfaces due to decreased viscosity and prolonged melting times. In contrast, a suppressed pulsed mode lowers energy input, reduces satellite formation, and improves vertical surfaces. Jamshidinia and Kovacevic[28] reported an inverse relationship between inter-wall gaps and roughness in electron-beam-melted thin plates, attributing higher roughness at small gaps to heat accumulation. Furthermore, surface roughness increased with the thickness of the powder layer between the walls. Examining three alloys, Wu *et al.*[9] demonstrated that thin-wall thickness is alloy-dependent, governed by thermophysical properties, material shrinkage, and inclination angles. Through *in situ* X-ray imaging of multilayer single-track melt pools, Bhatt *et al.*[29] observed that bi-directional multilayer scanning can lead to defects such as lapping and humping, which increase surface roughness.

Although the influence of processing parameters such as power and speed on vertical surface roughness in bulk geometries (e.g., cubes) has been thoroughly investigated, the relationship between surface roughness and dimensional accuracy in thin walls, representing a distinct class of additive manufacturing-preferred features, remains underexplored.[30] Key engineering aspects, including different scanning paths, orientations, and the coupled relationships among wall thickness, inter-wall gap, and dimensional error (DE), have yet to be systematically investigated. This study addresses these gaps by examining how LPBF process conditions affect vertical surface roughness and dimensional accuracy in thin walls and their intervening gaps. The underlying surface features and their formation mechanisms are analyzed to identify the root causes of surface roughness and their implications for dimensional accuracy. Furthermore, while cubic samples are often used for process parameters development, this work further compares melt pool morphology and surface quality between thin-wall and cubic geometries under identical laser parameters, providing insights into optimizing process parameters specifically for thin-wall structures.

2. Methodology

Thin-wall specimens were designed with nominal dimensions of 0.20 mm thickness, 3 mm height (height-to-thickness ratio of 15 to 1), and 10 mm length. Each build group consisted of three thin walls, producing two intervening gaps of equal nominal width. All thin walls were supported on a common base, as shown in Figure 1.

Gas-atomized 316L stainless steel powder (Carpenter Technology, Germany) was used as the feedstock. The chemical composition is presented in Table 1. The particle size distribution ranges from 15 to 45 μm, with an average particle size of 30 μm. Figure 2 shows the powder morphology, emphasizing the sphericity of the powder.

Based on previous studies,[31,32] an unstable cross-sectional ellipse-shaped melt pool transforms into a stable half-ellipse melt pool as the laser power increases from 260 W to 620 W, at a constant laser scanning speed of 1,466.6 mm/s in cube samples. Consequently, the top surface quality improved with increasing power due to the elimination of melt pool instability and discontinuity. To investigate the impact of the melt pool morphology on surface quality in thin walls, the same scan speed (1,466.6 mm/s) was used with three power settings: 260 W, 440 W, and 620 W. For each power, three groups of thin walls were fabricated under identical parameters within each group, shown in Figures 1 and 3. To evaluate the effect of gap distance on dimensional accuracy, three nominal

Table 1. The nominal chemical composition (wt.%) of stainless steel 316L

Element	Iron	Nickel	Chromium	Oxygen	Silicon	Sulfur	Phosphorus	Nitrogen	Carbon	Molybdenum	Manganese	Copper
Wt.%	Balance	12.7	17.7	0.03	0.62	0.01	0.01	0.10	0.02	2.36	0.65	0.02

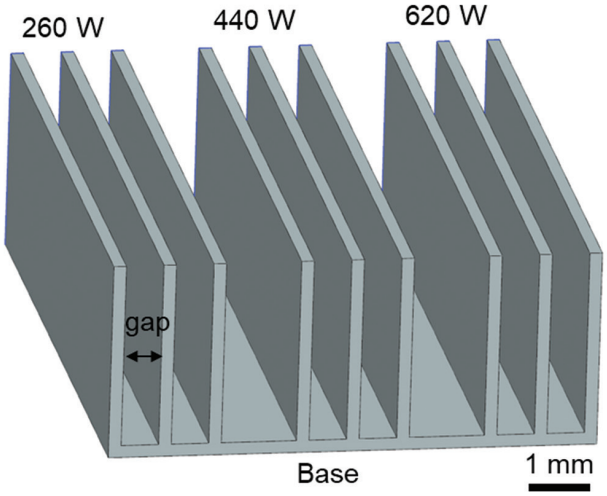

Figure 1. The thin-wall geometry design. Scale bar: 1 mm.

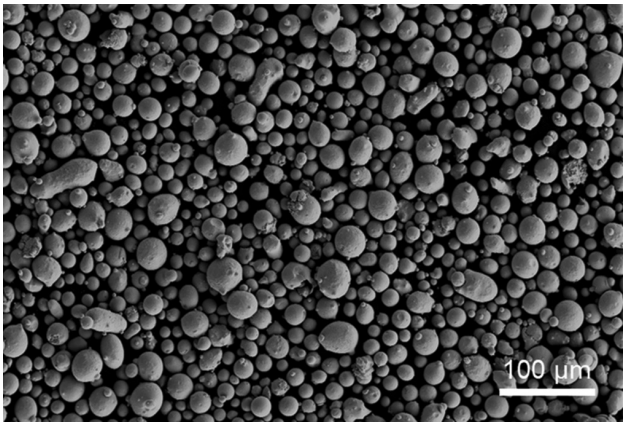

Figure 2. The powder morphology through scanning electron microscopy of 316L stainless steel. Scale bar: 100 µm; magnification: 1000×.

inter-wall gaps were designed, namely, 0.2 mm, 0.4 mm, and 0.6 mm (Figure 3).

As contour scans have been generally applied to control the surface roughness, two scan paths were employed, one with and one without contours. As illustrated in Figure 4A, in Scan Path 1, only hatch scans were utilized, where the hatch scans (red lines) extend to the geometry boundary. In Scan Path 2, the hatch scans offset inward by 50 µm, followed by a contour scan along the boundary using the same power and speed. In both scan paths, successive layers were rotated by 90°. Two orthogonal build orientations relative to the gas-flow/recoating

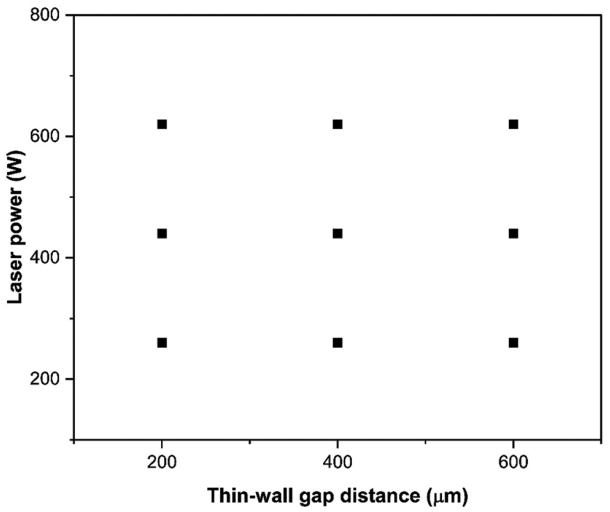

Figure 3. Experimental parametric design

direction were also tested: Parallel and perpendicular, as shown in Figure 4B.

Sample names followed the format P*_G*_S*_R, where P is power (W), G is gap distance (µm), S is scanning path, and R denotes perpendicular orientation to gas flow (e.g., P260_G200_S1_R indicates 260 W, Scan Path 1, 200 µm gap, and perpendicular orientation).

All builds were produced on an AconityMIDI LPBF system (United States) equipped with a single-mode fiber laser (maximum power 1,000 W). The laser spot diameter and hatch spacing were fixed at 100 µm, with a layer thickness of 30 µm. Laser scans were conducted with skywriting to minimize the impact of laser acceleration and deceleration.[33] During the printing, an argon atmosphere with oxygen levels below 100 ppm was maintained. Each condition was printed in duplicates to validate repeatability. All specimens were fabricated at ambient room temperature.

To assess the melt pool behavior on the thin-wall samples, top-down optical images were captured using the Keyence VHX 5000 digital optical microscope (Japan). An example is shown in Figure 5A. The samples were then sectioned perpendicular to the top layer track direction, followed by potting, polishing, and etching using a solution of 75 vol% hydrochloric acid and 25 vol% nitric acid for 15 s. Images were then acquired, offering a detailed depiction of the surface features of the thin-wall geometry,

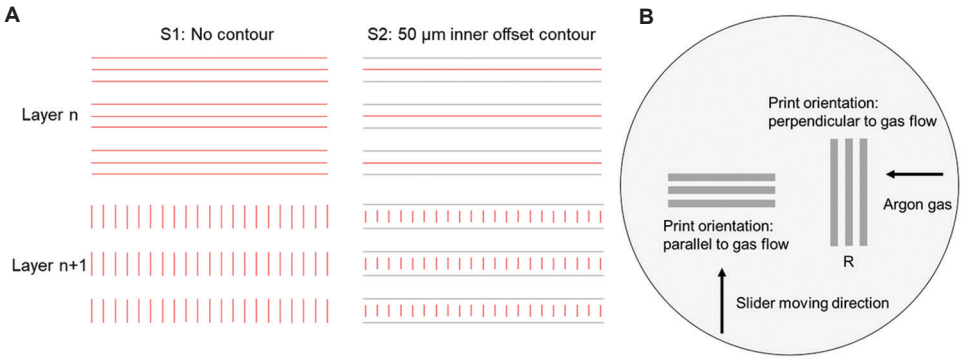

Figure 4. Illustration of printing setup: (A) different scan paths and (B) different print orientations

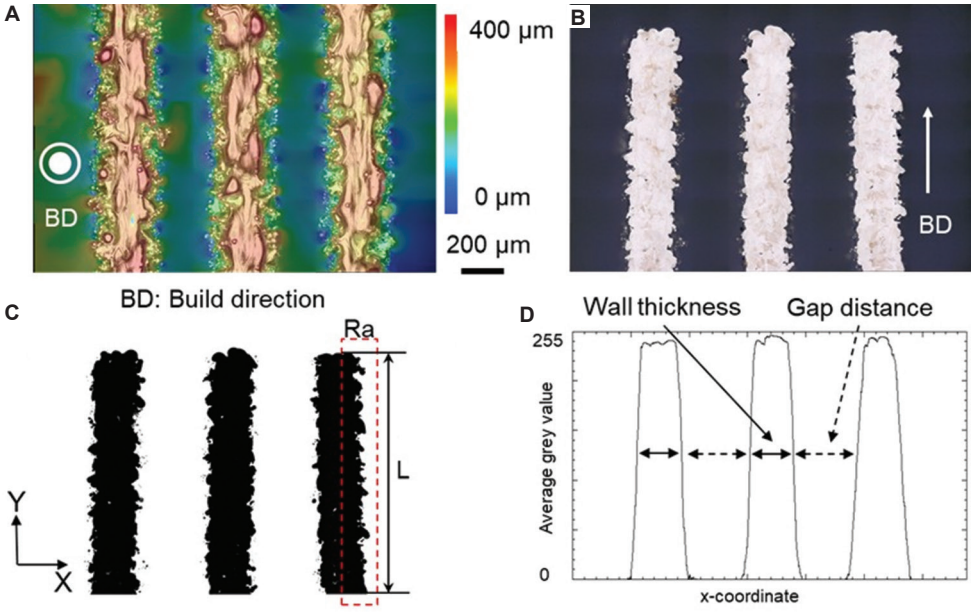

Figure 5. Characterization of thin-wall structures. (A) The topography of thin walls from the top-down view, (B) cross-sections, (C) the binarized image of (B), and (D) the continuous distribution map of average grey value along the x-axis based on (C). Scale bar: 200 μm; magnification: 500×.

as shown in Figure 5B. The images were then binarized to distinguish thin-wall and gap regions, as exemplified in Figure 5C. An average continuous grey value distribution along the x-axis was calculated and shown in Figure 5D. The average wall thickness or gap distance was measured from the average grey value 128 (half of the highest value 256). Multiple measurements were taken to account for measurement error with the standard deviation, as marked in Figure 5D. In addition to the dimensional measurements, surface roughness of vertical surfaces, quantified by Ra (arithmetic mean deviation of the roughness profile from the mean line), was calculated from the side-wall profile outlines, as expressed in Equation I:

$$Ra = \frac{1}{L}\int_0^L \left|x(y)\right| dy \quad \text{(I)}$$

where L means the nominal length of the outline, and x(y) denotes the local deviation of the surface from the mean profile position along the vertical (Y) direction. For example, to calculate the Ra of the vertical line highlighted in Figure 5C, the x-coordinate of the outline of the surface was obtained directly from the binarized cross-sectional image. Then, x(y) was calculated by subtracting the mean values of all x values from the local x-coordinate. For each process condition, the Ra values for six surface outlines were calculated, and the mean value and its standard deviation are reported. Note that the top-surface Ra was not quantified in this study due to the inherent strong stochastic variations caused by local melt pool instability under thin-wall conditions.

For comparison, 10 × 10 × 10 mm^3 cube samples were printed using the same laser parameters with a hatch

spacing of 100 μm and a hatch-contour offset of 50 μm (Scan Path 2) and characterized identically to thin walls.

3. Result and discussion

DE, defined by the difference between the measured and the nominal dimensions, is utilized to reflect the dimensional accuracy. For example, the thin-wall DE equals the measured wall thickness minus the constant design wall thickness, and the intervening gap DE is calculated by the measured gap distance minus the nominal gap distance (e.g., 200, 400, or 600 μm). In this study, DE analysis was limited to wall thickness and inter-wall gaps, as these directly govern functional accuracy. DE values associated with wall height, which is primarily dictated by top-surface variations and layer count, were not considered. Given the large height-to-thickness ratio (>15) in this study, fluctuations in wall height are negligible compared with errors in vertical wall thickness and gap dimensions. Figure 6 summarizes the DE of printed thin walls and the intervening gaps across all build conditions. The interpretation of the results is discussed in detail, regarding the effects of power, scanning path, sample orientation, and gap distance.

3.1. Role of laser power on surface roughness and dimensional accuracy

As shown in Figure 6, thin-wall DE generally increases with laser power, while gap DE decreases proportionally, reflecting the increase in thin-wall thickness. As the laser power increased, the cross-sectional melt pool morphology transformed from a small ellipse shape to a larger half-ellipse shape with a larger overlapping region of surrounding melt pools. To examine the details, Figure 7 depicts the melt pool morphology and surface features under G600_S2 conditions. Meanwhile, the melt pool areas (calculated by the pixel size in each figure and decided by the melt pool width and depth) and the vertical surface Ra are presented in Table 2. The average melt pool area increased significantly from 3,842 μm² to 9,662 μm² as the

Table 2. Melt pool area and surface roughness of vertical surface for G200_S2 thin walls

Thin walls	Melt pool area (μm²)	Ra (μm)
P260_G200_S2	3,842±1,452	13.94±0.79
P440_G200_S2	6,399±996	19.32±0.36
P620_G200_S2	9,662±2,481	21.35±4.43

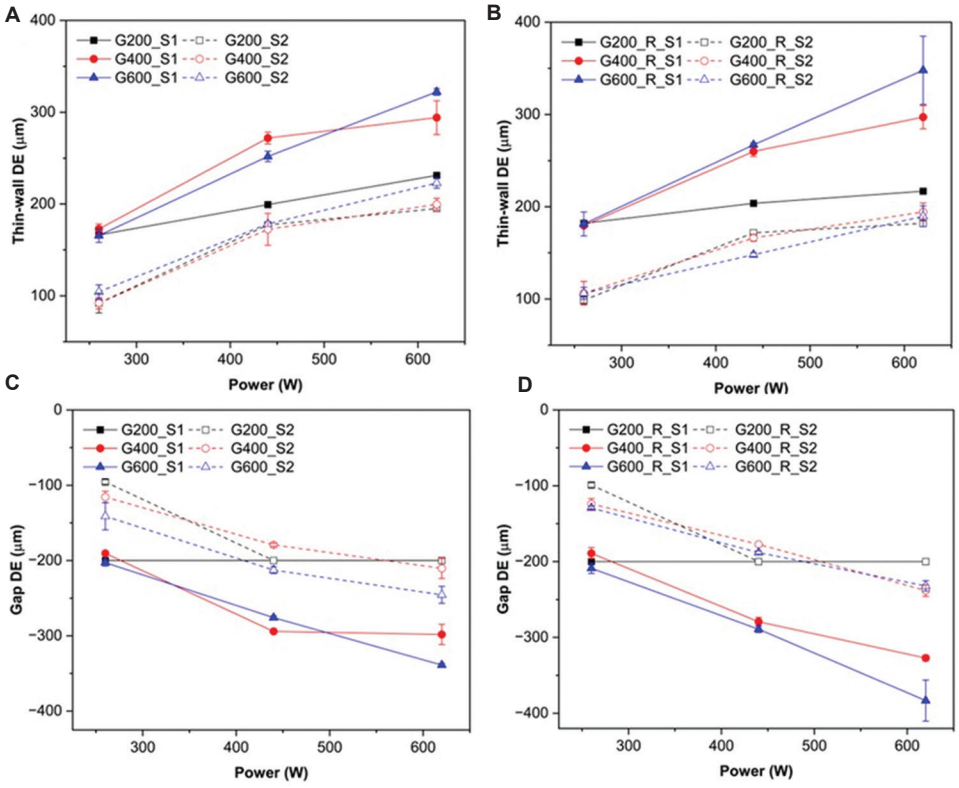

Figure 6. The DE as a function of the laser power. (A) Thin-wall DE for samples printed parallel to the gas flow, (B) thin-wall DE perpendicular to the gas flow, (C) DE of intervening gaps for samples printed parallel to the gas flow, and (D) DE of intervening gaps perpendicular to the gas flow.
Abbreviation: DE: Dimensional error.

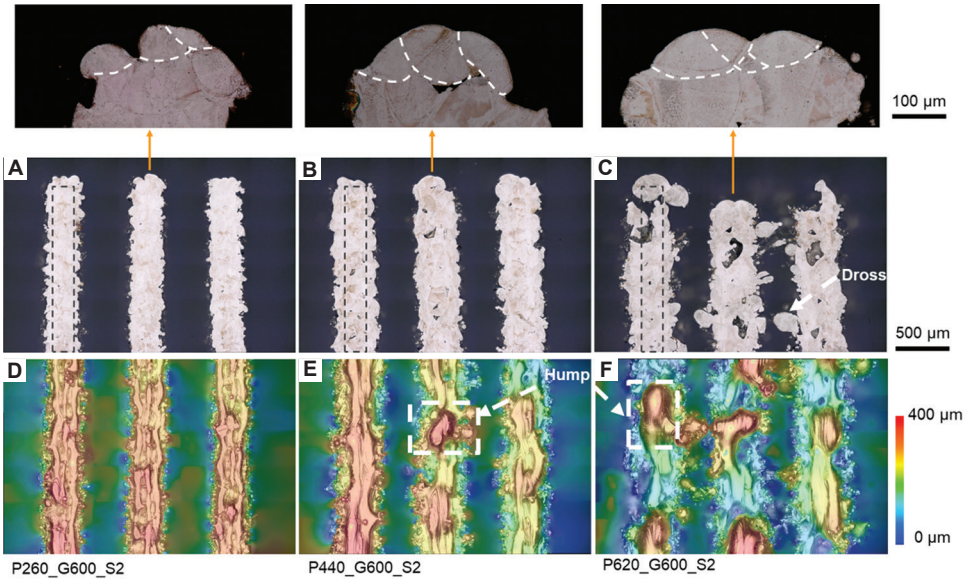

Figure 7. Thin-wall cross-sections (A-C) and topography for top surfaces (D-F) under group G600_S2 (the dashed line indicates the nominal geometry). (A and D) P260_G600_S2, (b and e) P440_G600_S2, (C and F) P620_G600_S2. Scale bar: 500 μm; magnification: 500×. The top row shows a zoomed-in view of the middle wall in each group. Scale bar: 100 μm; magnification: 1000×.

laser power increased from 260 W to 620 W. The increase in the melt pool size under higher laser power directly led to an increase in thin-wall thickness.

Higher power also alters vertical surface morphology. Enlarged melt pools promoted instability and spherical protrusion formation, increasing Ra from 13.94 μm to 21.35 μm. With low laser power at 260 W, a stable melt pool led to a better surface finish, where the melt tracks and partially attached particles dominated the side surface features (Figure 7A). As the power increases, the surface roughness worsens. Protrusions, as seen in Figure 7B and C, are typically referred to as the dross.[34,35] They dominate the side surface quality at 620 W conditions. The formation of dross is attributed to the asymmetric heat dissipation near the surface region. Since powder between walls impedes heat dissipation, it resulted in an asymmetric and large melt pool.[36] As the powder is absorbed by the melts and the physical support from the powder base diminishes, the enlarged melt pool migrates toward it, promoting the formation of dross.[37] As observed in Figure 7C, dross protruded beyond the intended thin-wall geometry, further supporting that the melt pool migration is responsible for its formation and the resultant rough surfaces. Consequently, average wall thickness rose from 304.3 μm to 422.9 μm (DE = 104.3 μm to 222.9 μm) between 260 W and 620 W.

3.2. Role of scan path

As shown in Figure 6A and B, thin-wall DEs manufactured without contour scanning (Scan Path 1, solid lines, ranging from 165.6 μm to 347.8 μm) consistently surpassed those produced with a 50 μm offset distance contour (Scan Path 2, dashed lines, ranging from 91.9 μm to 199.7 μm). Consequently, the gap DE without contour was constantly lower (solid lines in Figure 6C and D). As an example, with a fixed gap distance of 400 μm, the samples with Scan Path 1 (Figure 8A-C) have thicker walls than those under the Scan Path 2 (Figure 8D-F). The application of an inner offset, as shown in (Figure 4A) Scan Path 2 (S2), minimizes the scanning region and naturally compensates for the geometry expansion (melt pool extents out of the laser scanning paths). Larger overlaps with the inner hatches also restrict the melt pool migration, leading to less dross formation and better dimensional accuracy in the final products. In addition, the increase in thin-wall DE with rising laser power is evident in Figure 8. With and without contour scans, a more stable melt pool under low power conditions is preferred to minimize the expansion beyond the nominal geometry (Figure 8A and D). In contrast, higher power produces larger melt pools that not only increase wall thickness but also promote dross formation, thereby degrading surface quality (Figure 8C and D).

Such observation strongly indicates that the application of an inner offset can enhance printing precision in thin-wall geometries. Without or with a low offset distance, the melt pool naturally increases the thin-wall thickness. In contrast, an excessive offset distance may lead to a lack of fusion between contour and hatch scans, which could compromise the mechanical properties of the product.[22] The optimal contour offset is therefore strongly dependent

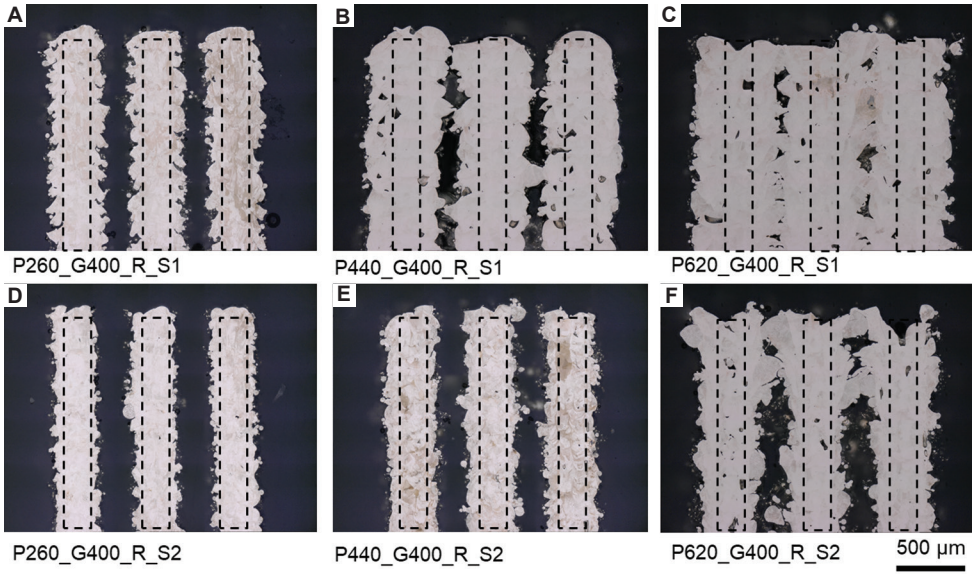

Figure 8. (A-F) Cross-section views of thin walls under different process conditions and scan paths. Scale bar: 500 µm; magnification: 500×.

on laser parameters. To balance vertical surface quality and fusion integrity, a relatively low energy density that is achieved through reduced power or increased scan speed should be used to suppress dross formation. Meanwhile, the offset distance should not exceed the combined melt pool widths of contour and hatch scans. For example, when using a low-power contour followed by low-power hatching, a smaller offset is recommended to avoid lack-of-fusion defects. In contrast, higher hatch energy density (e.g., high power) warrants both increased offset and contour power to mitigate dross formation from the hatch scans.

3.3. The impact of print orientation

Figure 6A and B show the thin-wall DEs printed in two orientations, both exhibiting a consistent increasing trend with laser power and a close proximity in the values of each data point across both orientations. A similar pattern is also observed in Figures 6C and D for gap DEs. The differences in thin-wall DEs between orientations are quantified in Figure 9A, which compares corresponding data points from Figure 6A and B. Across all gap sizes (black square = 200 µm, red dot = 400 µm, blue triangle = 600 µm) and both scan paths (solid and dashed lines), DE differences exhibited both negative and positive values and ranged from –33.2 µm to +33.2 µm. The maximal relative error was also < 9.5% of the overall thin-wall DE range (91.9–347.8 µm in Figure 6), including the measurement errors and process instabilities. This suggests that print orientation has only a limited influence on the dimensional accuracy of both thin walls and gaps.

To further validate the significance of print orientation statistically, a three-way analysis of variance was conducted on the DE data based on Scan Path 1 (data shown in Figure 6), with laser power (three levels), gap distance (three levels), and printing orientation (two levels) as factors. The results are summarized in Table 3. Both laser power (p<0.0001) and scan path (p=0.0053) were found to be statistically significant contributors to DE (the underlying mechanisms are discussed in Sections 3.1 and 3.3), while print orientation is not significant (p=0.5841). These findings quantitatively confirm the experimental observation that orientation effects are negligible in this study.

Both the magnitude and variability (error bars) of DEs increased with higher laser power for both thin walls and gaps, as shown in Figure 9A and B. This increase is likely due to greater melt pool instability at elevated power levels. Figure 10 presents cross-sectional views of thin walls fabricated with the two print orientations without contour scanning. Within each column of Figure 10, comparable dimensional accuracies and geometrical features are observed, with differences of < 4% between orientations, aligning with the trends in Figure 9. For example, at 260 W conditions, the surfaces are dominated by the melt track mitigations (Figure 10A and D). As the laser power increased, the wall gaps diminished, with voids randomly distributed between walls (Figure 10C and D). Although previous studies have reported that the slider recoating direction impacts the powder size distribution,[38,39] the results in this study suggest that both recoating direction and gas flow direction exert limited influence on the final geometric accuracy of thin walls and intervening gaps.

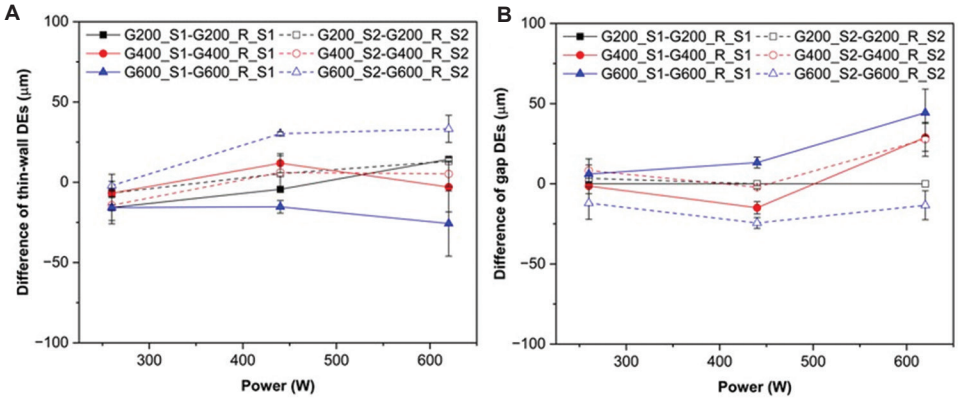

Figure 9. The difference in DEs between the two printing orientations. (A) Thin-wall thickness and (B) gap distance.
Abbreviation: DE: Dimensional error.

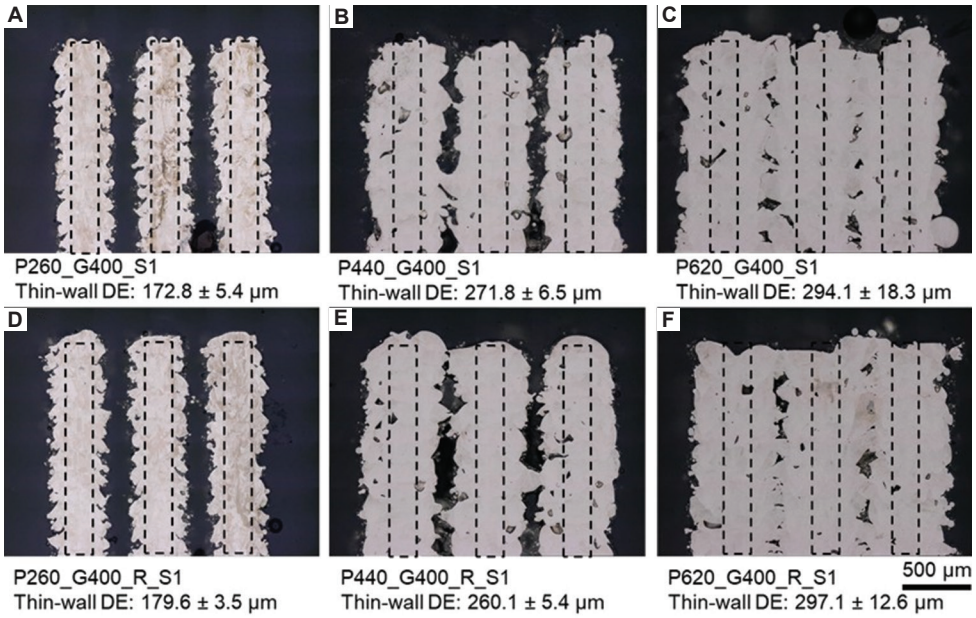

Figure 10. (A-D) Optical images of samples from cross-section view with print orientations parallel or perpendicular to the gas flow direction. Scale bar: 500 μm; magnification: 500×.
Abbreviation: DE: Dimensional error.

Table 3. Three-way analysis of variance for dimensional error

Source	Sum of squares	Degrees of freedom	Mean square	*F*	*p* (Prob > *F*)
Laser power	37,085.5	2	18,542.8	28.98	<0.0001
Gap distance	10,718.5	2	5,359.3	8.38	0.0053
Orientation	202.5	1	202.5	0.32	0.5841

3.4. The impact of gap distance

Three nominal gap distances (0.2 mm, 0.4 mm, and 0.6 mm) were examined to assess their influence on dimensional accuracy. Figure 11 shows the increase in melt pool migration as the gap distance widens under P440_R_S1 and P620_R_S1 conditions. At the smallest gap (0.2 mm in Figure 11A and D), adjacent walls coalesce at high laser power, restricting inward melt pool expansion. Under such conditions, the designed gap is eliminated entirely, representing a functional failure of the part. As the nominal gap increases, the constraint on melt pool

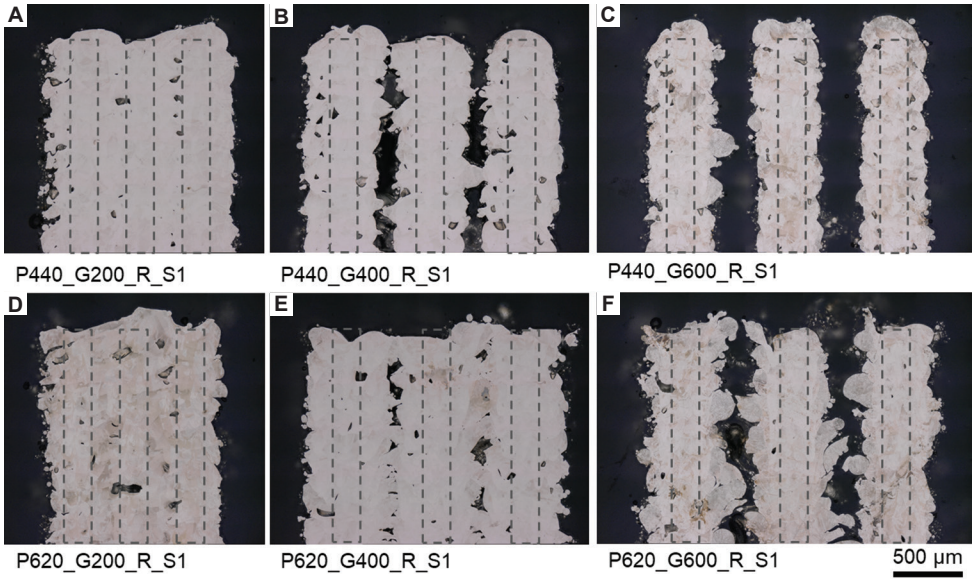

Figure 11. (A-F) Cross-sectional view under different nominal gap distances. Scale bar: 500 µm; magnification: 500×.

migration decreases, enabling more pronounced lateral flow and dross formation along the vertical surfaces. This increased thin-wall DE and slowed gap widening, resulting in smaller gap DE values (Figure 6C and D).

Given that the absolute values of DE at G200 were lower, but the gap was closed, Figure 12 presents the relative DEs for the gaps printed with two different orientations. At large gaps and high power, for example, P620_G600_R_S1 (Figure 11F), the actual gap was 216.7 µm, corresponding to an absolute DE of –383.3 µm (–64% relative DE). At smaller gaps, absolute DE decreased (–200 µm at G200), but relative DE reached –100% due to wall coalescence. This highlights that the final actual gap distance is determined by the extent of melt pool migration (especially at high power conditions) and the nominal gap distance, suggesting that a suitable design tolerance should be considered based on print conditions. To further provide general guidance, the final gap distance can be estimated as (Equation II):

$$D_g = D_N - D_{offset} - D_w \quad \text{(II)}$$

where the D_g denotes the final gap distance between thin walls, D_N is the nominal gap distance, D_{offset} is the contour offset distance (negative value as inward offset and positive value for outward offset) or the distances of the outermost hatch line from the nominal wall boundary if no contour is applied, and D_w is the melt pool width of the contour scan or outermost hatch track.

Under an ideal scenario, when the inward offset equals the melt pool width, $D_g = D_N$, resulting in minimal error. Note that, at high energy density (e.g., 620 W, 1,466.6 mm/s in this study), contour scans promote dross formation, which leads to large variations in surface roughness (exemplified in Figure 7C). To reduce the gap distance error and its variability, low energy density conditions with reduced laser power are recommended (e.g., 260W, 1,466.6 mm/s in Figure 7A). However, when hatch scans are conducted at high power conditions, low-energy contour scans may not fully overlap with the hatch tracks. In such cases, an increased inward offset distance would be applied to accommodate the extension of the hatch melt pool beyond the contour track.

While the present work was conducted at a fixed scan speed, hatch spacing, and layer thickness, the representative process parameters under different laser power illustrate three representative regimes of vertical-surface formation:[40] (i) Stable melt pools dominated by partially melted particles, (ii) Highly unstable melt pools where lateral migration produces dross, and (iii) Intermediate states between the two. Although the exact roughness values and wall thickness will vary under different process windows, the underlying mechanisms by which melt pool behaviors govern vertical surface quality and accuracy remain broadly valid. In this context, the guideline to reduce the DE, such as adopting an appropriate inward contour offset based on the melt pool behavior, is applicable to different process conditions.

The data in Figure 12A and B show minimal differences between orientations, reinforcing the earlier conclusion that print orientation plays a limited role. Moreover, the impact of the nominal wall distance on heat accumulation and melt pool temperature (expansion and migration) has been found to be limited due to the

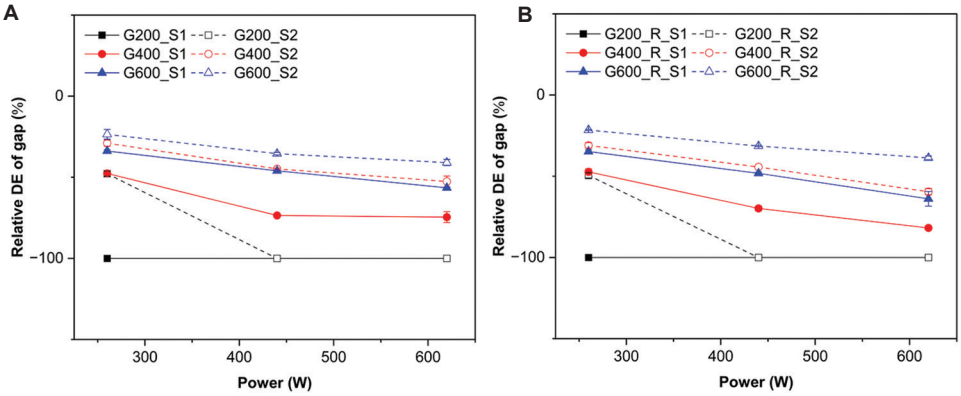

Figure 12. Relative DE of thin-wall structures: (A) gap printed parallel to the gas flow direction, and (B) gap printed perpendicularly to the gas flow direction
Abbreviation: DE: Dimensional error.

similarity of melt pool dimensions in different nominal gap distance conditions.

3.5. Surface characteristics in thin walls and cubes

In addition to vertical surfaces, the top-surface quality and dimensional accuracy are also important performance metrics, yet are rarely discussed. As seen in Figures 7, 8, 10, and 11, the 260 W condition produces insufficient energy input, resulting in disconnected melt tracks and valley formation that dominate the top surface. At higher laser powers, such as 440 W and 620 W, large humps, approximately 200 µm in height, form on the top surface and dominate the top surface feature, as marked in Figure 7E and F. These humps originate from melt pool migration from previous tracks, which disrupts uniform powder distribution in the subsequent layers, reduces melt pool stability for the later tracks, and degrades surface quality.[2,32]

In contrast to previous studies,[31,32] where higher laser power improved top-surface finish in cube samples, the present work observes opposite behavior for thin walls. To verify these differences, 10 × 10 × 10 mm^3 cube samples were fabricated using identical parameters. As shown in Figure 13, the larger melt pool and overlapping region in cube samples reduce the melt pool instability and smooth the top surface (Ra decreasing from 31.27 µm to 12.06 µm) with the laser power increases (260 W to 620 W). This improvement arises from enhanced wetting between melt pools and prior layers, aided by larger contact areas, lower viscosity, and longer solidification times that promote gravity-driven leveling and centrifugal Marangoni flow (under low sulfur and oxygen content in stainless steel[41]). In addition, repeated remelting from subsequent high-power scans further smooth the surface by eliminating the top surface

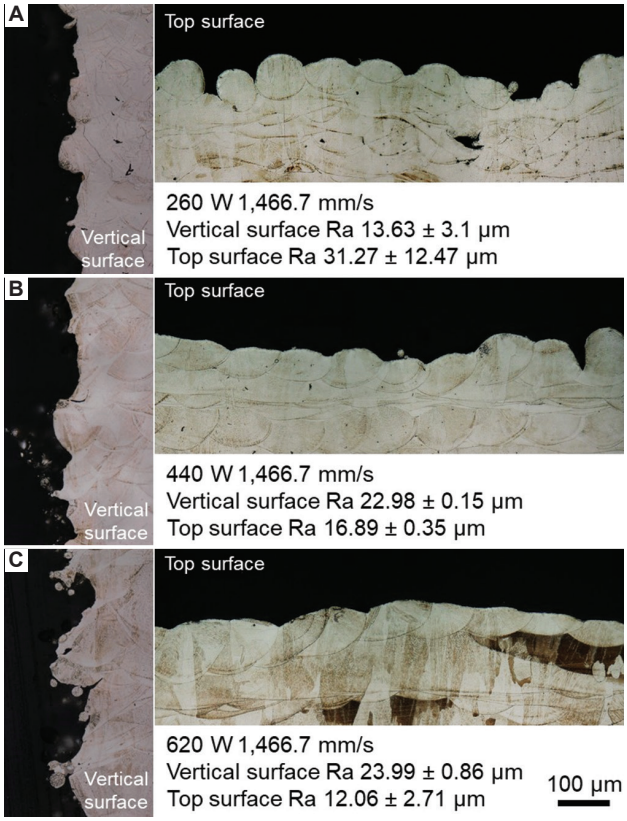

Figure 13. The cross-sectional views of the top and vertical surface regions of the cube samples. (A) 260W 1,466.7 mm/s, (B) 440 W 1,466.7 mm/s, (C) 620 W 1,466.7 mm/s. Scale bar: 100 µm; magnification: 1000×.

humps. However, these stabilizing and remelting effects are absent in thin-wall builds. The limited number of scan tracks amplifies track-to-track interactions and produces large variations in melt pool dimensions due to pronounced local geometry changes, which in turn alter solidification conditions. Melt pool migration, combined

with possible powder denudation at vertical edges, could also lead to uneven powder distribution near thin walls, further disrupting melt pool stability at the top surface and resulting in a poorer top surface finish, as shown in Figure 7C and F. Increasing wall thickness promotes melt pool stabilization as the melt progresses, explaining why cube samples exhibit improved top surfaces under higher power while thin walls do not.

For vertical surfaces, however, both cubes and thin walls exhibited similar trends: Ra increased with laser power due to dross formation, rising from 13.61 μm to 23.99 μm in cubes and from 13.94 μm to 21.35 μm in thin walls. This similarity suggests that cube samples can serve as a useful proxy for optimizing vertical-surface quality and dimensional accuracy in thin-wall manufacturing. Notably, surface quality and dimensional accuracy are more critical on vertical surfaces compared to top surfaces in thin-wall applications.

Overall, achieving better dimensional accuracy in thin-wall geometries and their intervening gaps requires careful integration of print conditions and design parameters. As sufficient energy for hatch scans must be maintained to achieve fully dense walls, an appropriate hatch-contour offset can minimize thin-wall DE. To achieve a desired intervening gap dimension, the melt pool expansion and migration need to be accommodated with the designed contour offset distance, particularly in high-power contour scans. This is especially important when rougher surface quality is acceptable or preferred for specific applications.

4. Conclusion

This study systematically examined the effects of laser power, scanning paths, print orientation, and nominal gap distance on surface quality and dimensional accuracy in thin-wall structures of 316L stainless steel in LPBF. Dominant surface characteristics and their formation mechanisms were identified for both top and vertical surfaces and direct comparisons were made with cube geometries fabricated under identical process conditions.

Higher power and larger scanned areas increased vertical surface roughness and DE due to melt pool migration and dross formation. Dross protrusions at wall edges provided direct evidence of lateral melt pool movement along vertical surfaces. In addition, applying a modest inward hatch offset with a contour scan reduced melt pool migration, suppressed dross formation, and improved dimensional accuracy. Offsets that are too small permit overbuilding, while excessive offsets risk lack-of-fusion defects; optimal values should reflect laser energy density and melt pool width.

Orientation relative to the gas-flow/recoating direction had a negligible influence on dimensional accuracy or surface quality under the tested conditions. The actual gap size was jointly determined by melt pool migration and the nominal design. Small gaps may close entirely under high-power conditions, while larger gaps remain open but are reduced by lateral melt flow. Appropriate design tolerances are essential, especially for high-energy scans.

In high-power conditions, cube samples exhibited smoother top surfaces than thin walls due to improved melt pool wetting, larger overlap, and repeated remelting. Thin walls lack these stabilizing effects due to denudation and powder redistribution near vertical edges, leading to reduced top-surface quality. Vertical surface roughness trends, however, were similar in both geometries, making cubes a suitable proxy for optimizing side-wall conditions.

These results clarify the interplay between processing parameters, geometry, and feature spacing in determining surface roughness and dimensional accuracy in thin-wall LPBF. They provide a framework for localized process control, enabling geometry-specific optimization of surface quality and dimensional accuracy to meet functional requirements in complex additive manufacturing components.

Acknowledgments

None.

Funding

The authors would like to acknowledge the support from the National Science Foundation under grant number 2029425, the U.S. Department of Commerce, the National Institute of Standards and Technology under grant number 70NANB23H030, and the U.S. Department of Energy, Savannah River National Laboratory under contract no. 89303321CEM000080.

Conflict of interest

Lang Yuan is an Editorial Board Member of this journal but was not in any way involved in the editorial and peer-review process conducted for this paper, directly or indirectly. Separately, the other author declared that he/she has no known competing financial interests or personal relationships that could have influenced the work reported in this paper.

Author contributions

Conceptualization: Lang Yuan
Formal analysis: Tianyu Zhang
Funding acquisition: Lang Yuan
Investigation: Tianyu Zhang
Methodology: All authors
Supervision: Lang Yuan
Writing–original draft: Tianyu Zhang
Writing–review & editing: All authors

Ethics approval and consent to participate

Not applicable.

Consent for publication

Not applicable.

Availability of data

All data analyzed have been presented in the paper.

References

1. Yakout M, Cadamuro A, Elbestawi MA, Veldhuis SC. The selection of process parameters in additive manufacturing for aerospace alloys. *Int J Adv Manuf Technol*. 2017; 92(5-8):2081-2098.

   doi: 10.1007/s00170-017-0280-7

2. Jing G, Wang Z. Defects, densification mechanism and mechanical properties of 300M steel deposited by high power selective laser melting. *Addit Manuf*. 2021;38:101831.

   doi: 10.1016/j.addma.2020.101831

3. Gu DD, Meiners W, Wissenbach K, Poprawe R. Laser additive manufacturing of metallic components: Materials, processes and mechanisms. *Int Mater Rev*. 2012;57(3):133-164.

   doi: 10.1179/1743280411Y.0000000014

4. DebRoy T, Wei HL, Zuback JS, *et al*. Additive manufacturing of metallic components - Process, structure and properties. *Prog Mater Sci*. 2018;92:112-224.

   doi: 10.1016/j.pmatsci.2017.10.001

5. Rastan H, Abdi A, Hamawandi B, Ignatowicz M, Meyer JP, Palm B. Heat transfer study of enhanced additively manufactured minichannel heat exchangers. *Int J Heat Mass Transf*. 2020;161:120271.

   doi: 10.1016/j.ijheatmasstransfer.2020.120271

6. Tian B, Chang W, Santi E, Li C, Zhang T, Yuan L. Two-Phase Milli/Microchannel Cooling for SiC Power Module Using Dielectric Fluid Coolant. In: *2021 IEEE Electric Ship Technologies Symposium, ESTS 2021*. 2021.

   doi: 10.1109/ESTS49166.2021.9512324

7. Chakraborty A, Tangestani R, Esmati K, Sabiston T, Yuan L, Martin É. Mitigating inherent micro-cracking in laser additively manufactured RENÉ 108 thin-wall components. *Thin Walled Struct*. 2023;184:110514.

   doi: 10.1016/J.TWS.2022.110514

8. Kaur I, Singh P. State-of-the-art in heat exchanger additive manufacturing. *Int J Heat Mass Transf*. 2021;178:121600.

   doi: 10.1016/J.IJHEATMASSTRANSFER.2021.121600

9. Wu Z, Narra SP, Rollett A. Exploring the fabrication limits of thin-wall structures in a laser powder bed fusion process. *Int J Adv Manuf Technol*. 2020;110(1-2):191-207.

   doi: 10.1007/s00170-020-05827-4

10. Mehrabi O, Seyedkashi SMH, Moradi M. Functionally graded additive manufacturing of thin-walled 316L stainless steel-inconel 625 by direct laser metal deposition process: Characterization and evaluation. *Metals (Basel)*. 2023;13(6):1108.

    doi: 10.3390/met13061108

11. Feng Z, Wang G, Hao Z, *et al*. Influence of scale effect on surface morphology in laser powder bed fusion technology. *Virtual Phys Prototyp*. 2024;19(1):e2336157.

    doi: 10.1080/17452759.2024.2336157

12. Poncelet O, Marteleur M, van der Rest C, *et al*. Critical assessment of the impact of process parameters on vertical roughness and hardness of thin walls of AlSi10Mg processed by laser powder bed fusion. *Addit Manuf*. 2021;38:101801.

    doi: 10.1016/J.ADDMA.2020.101801

13. Thompson SM, Aspin ZS, Shamsaei N, Elwany A, Bian L. Additive manufacturing of heat exchangers: A case study on a multi-layered Ti-6Al-4V oscillating heat pipe. *Addit Manuf*. 2015;8:163-174.

    doi: 10.1016/j.addma.2015.09.003

14. Zhang Z, Huang Y, Rani Kasinathan A, *et al*. 3-Dimensional heat transfer modeling for laser powder-bed fusion additive manufacturing with volumetric heat sources based on varied thermal conductivity and absorptivity. *Opt Laser Technol*. 2019;109:297-312.

    doi: 10.1016/j.optlastec.2018.08.012

15. Lee J, Hussain A, Ha J, *et al*. Mechanical properties of Ti-6Al-4V thin walls fabricated by laser powder bed fusion. *Addit Manuf*. 2024;94:104484.

    doi: 10.1016/J.ADDMA.2024.104484

16. Zhang J, Wang H. Magnetically driven internal finishing of AISI 316L stainless steel tubes generated by laser powder bed fusion. *J Manuf Process*. 2022;76:155-166.

    doi: 10.1016/j.jmapro.2022.02.009

17. Favero G, Berti G, Bonesso M, *et al*. Experimental and numerical analyses of fluid flow inside additively manufactured and smoothed cooling channels. *Int Commun*

Heat Mass Transfer. 2022;135:106128.

doi: 10.1016/J.ICHEATMASSTRANSFER.2022.106128

18. Cao L, Li J, Hu J, Liu H, Wu Y, Zhou Q. Optimization of surface roughness and dimensional accuracy in LPBF additive manufacturing. *Opt Laser Technol*. 2021;142:107246.

doi: 10.1016/j.optlastec.2021.107246

19. Wang D, Yang Y, Yi Z, Su X. Research on the fabricating quality optimization of the overhanging surface in SLM process. *Int J Adv Manuf Technol*. 2013;65(9-12):1471-1484.

doi: 10.1007/s00170-012-4271-4

20. Lu Z, Tan MJ, Zhang Y, An J, Chua CK. Impact of machine factors on the surface quality of parts fabricated via powder bed fusion. *Eng Sci Addit Manuf*. 2025;1(2):025240014.

doi: 10.36922/ESAM025240014

21. Feng S, Kamat AM, Sabooni S, Pei Y. Experimental and numerical investigation of the origin of surface roughness in laser powder bed fused overhang regions. *Virtual Phys Prototyp*. 2021;16(S1):S66-S84.

doi: 10.1080/17452759.2021.1896970

22. Zhang T, Yuan L. Interaction of contour and hatch parameters on vertical surface roughness in laser powder bed fusion. *J Mater Res Technol*. 2024;32:3390-3401.

doi: 10.1016/j.jmrt.2024.08.170

23. Klingaa CG, Dahmen T, Baier S, Mohanty S, Hattel JH. X-ray CT and image analysis methodology for local roughness characterization in cooling channels made by metal additive manufacturing. *Addit Manuf*. 2020;32:101032.

doi: 10.1016/j.addma.2019.101032

24. Klingaa CG, Dahmen T, Baier-Stegmaier S, Mohanty S, Hattel JH. Investigation of the roughness variation along the length of LPBF manufactured straight channels. *Nondestr Test Eval*. 2020;35(3):304-314.

doi: 10.1080/10589759.2020.1785445

25. Gockel J, Sheridan L, Koerper B, Whip B. The influence of additive manufacturing processing parameters on surface roughness and fatigue life. *Int J Fatigue*. 2019;124:380-388.

doi: 10.1016/j.ijfatigue.2019.03.025

26. Patel S, Rogalsky A, Vlasea M. Towards understanding side-skin surface characteristics in laser powder bed fusion. *J Mater Res*. 2020;35(15):2055-2064.

doi: 10.1557/jmr.2020.125

27. Mumtaz KA, Hopkinson N. Selective laser melting of thin wall parts using pulse shaping. *J Mater Process Technol*. 2010;210(2):279-287.

doi: 10.1016/j.jmatprotec.2009.09.011

28. Jamshidinia M, Kovacevic R. The influence of heat accumulation on the surface roughness in powder-bed additive manufacturing. *Surf Topogr*. 2015;3(1):014003.

doi: 10.1088/2051-672X/3/1/014003

29. Bhatt A, Huang Y, Leung CLA, *et al*. In situ characterisation of surface roughness and its amplification during multilayer single-track laser powder bed fusion additive manufacturing. *Addit Manuf*. 2023;77:103809.

doi: 10.1016/j.addma.2023.103809

30. Vu HM, Meiniger S, Ringel B, *et al*. Investigation on surface characteristics of wall structures out of stainless steel 316L manufactured by laser powder bed fusion. *Prog Addit Manuf*. 2024;9(6):2041-2060.

doi: 10.1007/S40964-023-00559-9/FIGURES/15

31. Zhang Z, Zhang T, Sun C, Karna S, Yuan L. Understanding melt pool behavior of 316L stainless steel in laser powder bed fusion additive manufacturing. *Micromachines (Basel)*. 2024;15(2):170.

doi: 10.3390/mi15020170

32. Zhang T, Yuan L. Melt pool characteristics on surface roughness and printability of 316L stainless steel in laser powder bed fusion. *Rapid Prototyp J*. 2024.

doi: 10.1108/RPJ-02-2024-0078

33. Tian Y, Tomus D, Rometsch P, Wu X. Influences of processing parameters on surface roughness of Hastelloy X produced by selective laser melting. *Addit Manuf*. 2017;13:103-112.

doi: 10.1016/j.addma.2016.10.010

34. Charles A, Bayat M, Elkaseer A, Thijs L, Hattel JH, Scholz S. Elucidation of dross formation in laser powder bed fusion at down-facing surfaces: Phenomenon-oriented multiphysics simulation and experimental validation. *Addit Manuf*. 2022;50:102551.

doi: 10.1016/j.addma.2021.102551

35. Charles A, Elkaseer A, Paggi U, Thijs L, Hagenmeyer V, Scholz S. Down-facing surfaces in laser powder bed fusion of Ti6Al4V: Effect of dross formation on dimensional accuracy and surface texture. *Addit Manuf*. 2021;46:102148.

doi: 10.1016/j.addma.2021.102148

36. Wrobel R, Del Guidice L, Scheel P, *et al*. Influence of wall thickness on microstructure and mechanical properties of thin-walled 316L stainless steel produced by laser powder bed fusion. *Mater Des*. 2024;238:112652.

doi: 10.1016/j.matdes.2024.112652

37. Zhang T, Yuan L. Understanding surface roughness on vertical surfaces of 316 L stainless steel in laser powder bed fusion additive manufacturing. *Powder Technol*. 2022;411:117957.

doi: 10.1016/j.powtec.2022.117957

38. Mussatto A, Groarke R, O'Neill A, Obeidi MA, Delaure Y, Brabazon D. Influences of powder morphology and spreading parameters on the powder bed topography uniformity in

powder bed fusion metal additive manufacturing. *Addit Manuf*. 2021;38:101807.

doi: 10.1016/j.addma.2020.101807

39. Averardi A, Cola C, Zeltmann SE, Gupta N. Effect of particle size distribution on the packing of powder beds: A critical discussion relevant to additive manufacturing. *Mater Today Commun*. 2020;24:100964.

doi: 10.1016/j.mtcomm.2020.100964

40. Snyder JC, Thole KA. Understanding laser powder bed fusion surface roughness. *J Manuf Sci Eng Trans ASME*. 2020;142(7):1071003.

doi: 10.1115/1.4046504/1074958

41. Leung CLA, Marussi S, Towrie M, Atwood RC, Withers PJ, Lee PD. The effect of powder oxidation on defect formation in laser additive manufacturing. *Acta Mater*. 2019;166:294-305.

doi: 10.1016/j.actamat.2018.12.027